Observation of Spatial Variability of Diurnal Thermocline and Rain-Formed Halocline in the Western Pacific Warm Pool

ALEXANDER SOLOVIEV AND ROGER LUKAS

Department of Oceanography, School of Ocean and Earth Science and Technology, University of Hawaii, Honolulu, Hawaii

22 August 1995 and 1 May 1996

ABSTRACT

High-resolution measurements of temperature and salinity were made in the near-surface layer of the ocean during the Tropical Oceans-Global Atmosphere Coupled Ocean–Atmosphere Response Experiment, using probes mounted on the bow of the R/V *Moana Wave*. Because of surface waves and pitching of the vessel, the bow probes profiled the near-surface layer of the ocean within depths of 0–4.0 m. In the near-surface layer of the ocean in the western Pacific warm pool, strong variability of temperature and salinity produced by diurnal heating and/or rain was often observed. The contoured density field revealed cases of pronounced spatial variability. The shallow diurnal thermocline and rain-formed halocline are subject to perturbations that sometimes look like large amplitude internal waves. Possible sources of the internal waves in the near-surface layer of the ocean are discussed.

1. Introduction

The western Pacific warm pool is a very sensitive region in the global climate system (Webster and Lukas 1992). A better understanding of the near-surface layer structure in this region is important for improving parameterization of subgrid-scale processes in coupled global circulation models. Diurnal heating and precipitation effects may result in strong stratification of the near-surface layer of the ocean, especially under calm weather conditions (Bruce and Firing 1974; Soloviev and Vershinsky 1982). Diurnal cycle and rain events may substantially influence the turbulent regime in the near-surface layer of the ocean (Brainerd and Gregg 1993; Smyth et al. 1995, manuscript submitted to *J. Phys. Oceanogr.*). Using 1D modeling, Anderson et al. (1995, manuscript submitted to *J. Climate*) demonstrated how the coupling of the diurnal cycle with precipitation effects in the near-surface layer of the ocean results in the formation of a "barrier layer," which is an intrinsic feature of the western Pacific warm pool (Lukas and Lindstrom 1991).

The dynamical processes in the near-surface layer of the ocean are often characterized and recognized by spatial structures (Thorpe 1995). The purpose of this note is to report new high-resolution observations of thermohaline spatial structures in the near-surface layer of the western Pacific warm pool made during the TOGA COARE.

This paper is organized as follows. Section 2 briefly describes the new instrumentation and techniques used for the measurements. Section 3 presents examples of observations of internal waves in the rain-formed halocline and diurnal thermocline. Section 4 briefly discusses two possible sources for the internal waves in the near-surface layer of the warm pool.

2. Instrumentation and techniques

The instrumentation installed on the bow of the R/V *Moana Wave* included an electrical conductivity–temperature–pressure probe (ECTP) and an electromagnetic velocity and acceleration probe (EMVA). The probes were mounted at ~1.7 m mean depth using a special frame. The ECTP probe contained a copper-wire temperature sensor, an inductive conductivity cell, and a strain-gauge pressure sensor. To reduce the influence of the dynamic component, the pressure sensor was placed in the rear of the bow probe. The EMVA probe included a three-component fluctuation-velocity electromagnetic sensor and two acceleration sensors. Further information about the bow probes is given in Table 1. Measuring, acquisition, and processing techniques are discussed below. A more detailed discussion of techniques and instrumentation can be found in Soloviev et al. (1995).

A special program was developed at the University of Hawaii for acquisition and preliminary processing of the bow sensor signals. We used sampling rates of 40 and 400 Hz. Surfacing of the probes and bubble patches disturb the conductivity measurement. Bubbles

Corresponding author address: Dr. Alexander V. Soloviev, c/o Prof. Roger B. Lukas, Department of Oceanography, University of Hawaii, MSB #419, 1000 Pope Road, Honolulu, HI 96822.
E-mail: soloviev@iniki.soest.hawaii.edu

TABLE 1. Main technical characteristics of bow probes in COARE EM (15 Mar–5 Apr 1994) and EQ-3 (11 Apr–11 May 1994) legs of the R/V *Moana Wave*.

Temperature	
Accuracy (°C)	0.1
Stability during 8 hours (°C)	<0.01
Digital resolution (°C)	0.005
Response time of primary sensor (ms)	35
Conductivity	
Accuracy (S/m)	0.01
Stability during 8 h (S/m)	<0.001
Digital resolution (S/m)	0.0012
Space resolution (m)	0.1
Pressure	
Accuracy (dbar)	0.1[a]
Digital resolution (dbar)	0.01
Longitudinal fluctuation velocity (V_x)	
Range (m s^{-1})	±2.5
Precision (%)	<5
Digital resolution (m s^{-1})	0.0011
Frequency range (Hz)	0.05–200

[a] After drift correction at probe surfacing.

may also disturb the temperature measurement (Farmer and Gemmrich 1996). An algorithm that automatically detects segments disturbed by the probes surfacing or by the bubble patches and removes them from the signals was developed (Soloviev et al. 1995). To compensate for $L = 8.4$ cm spatial separation between the temperature sensor and the conductivity cell in the ECTP, the conductivity signal is lagged by $\Delta t = L/U$, which is the time it takes for water to travel that distance. This varies with different relative flow speed U. At a ship speed of 5 m s^{-1}, the conductivity sensor had a much faster response than the temperature sensor. To match the phase shift and response time of the temperature and conductivity sensors in calculating salinity (Fozdar et al. 1985), the conductivity signal is processed by an exponential filter with a cutoff frequency of 4.547 Hz corresponding to a 35 ms response time for the temperature sensor. Before calculation of salinity and density both the temperature and conductivity signals were also filtered using a low-pass Hanning filter with a cutoff frequency of 4 Hz. Finally, the temperature, salinity, density, and pressure were decimated to the 8-Hz sampling rate. The hydrostatic pressure bias was removed within 10-min segments by subtracting the pressure sensor value when the probe is in the air. The conductivity was an indicator of the probe surfacing. If no surfacing occurred within a 10-min segment, the previous value was applied to remove the pressure bias.

At a ship speed of >2 m s^{-1}, the probes collected information from an undisturbed relative flow ahead of the moving vessel. Because of surface waves and associated pitching of the vessel, the bow probes profiled the near-surface layer of the ocean in the 0–4.0-m depth range. This provided a new opportunity to study both vertical and horizontal structure of the near-surface layer of the ocean. An rms uncertainty of <0.1 dbar in pressure to depth conversion at a ship speed of 10–11 knots was estimated using the pressure readings at occasional intersections of the water–air surface detected by the conductivity sensor (see appendix).

Simultaneous T–S measurements were made by the thermosalinograph system (SeaBird Electronics CTD SBE-21) of the R/V *Moana Wave* (Shinoda et al. 1995) by pumping water from the bow intake at 3-m depth. During the *Moana Wave* COARE EQ-3 cruise (30 days), the bow sensor temperature and salinity measurements within the pressure range of 2.8–3.2 dbar were averaged at 10-min time intervals and compared with the corresponding 10-min averages of the thermosalinograph temperature and salinity. The results of this comparison are as follows. An rms difference of 0.014 psu and a slowly varying mean difference change from −0.013 to 0.001 psu between the bow probe and the thermosalinograph were observed. This change can be partially explained by a drift of the ECTP temperature sensor. The mean temperature difference between the bow probe and the thermosalinograph thermistor at the 3-m intake changed from 0.034° to 0.057°C. The corresponding rms difference between the bow temperature probe and the thermosalinograph thermistor was equal to 0.012°C.

3. Observations in the western Pacific warm pool

Measurements by the bow sensors and the thermosalinograph were made in the western Pacific in 1993–94 during three TOGA COARE cruises on the R/V *Moana Wave* (Soloviev et al. 1995; Shinoda et al. 1995). Data obtained during the COARE EQ-3 cruise (11 April–11 May 1995) is used in this paper.

In the western Pacific warm pool, we often observed strongly stratified near-surface layers produced by rain and/or diurnal heating. Two examples of measurements made while steaming at 10–11 knots are shown in Figs. 1a,b. Averaged vertical profiles of temperature (T), salinity (S), and density (σ_t) are shown in Figs. 2a,b. They are calculated by sorting the data in pressure (P) and averaging over the 10-min time intervals, which are indicated on the time axis of Fig. 1 by heavy line segments. Segments marked by rectangles in Fig. 1 are shown in Figs. 3 and 4 in more detail.

a. Rain-formed halocline

Figure 1a shows P, T, S, and σ_t for a time series during an intersection of a low salinity patch. This low salinity is associated with the strong rain event observed in this area. This patch is also traced on the temperature record because the temperature of the rain droplets is lower than SST. High-frequency fluctuations of T, S, and σ_t are primarily because of the depth variation of the probes.

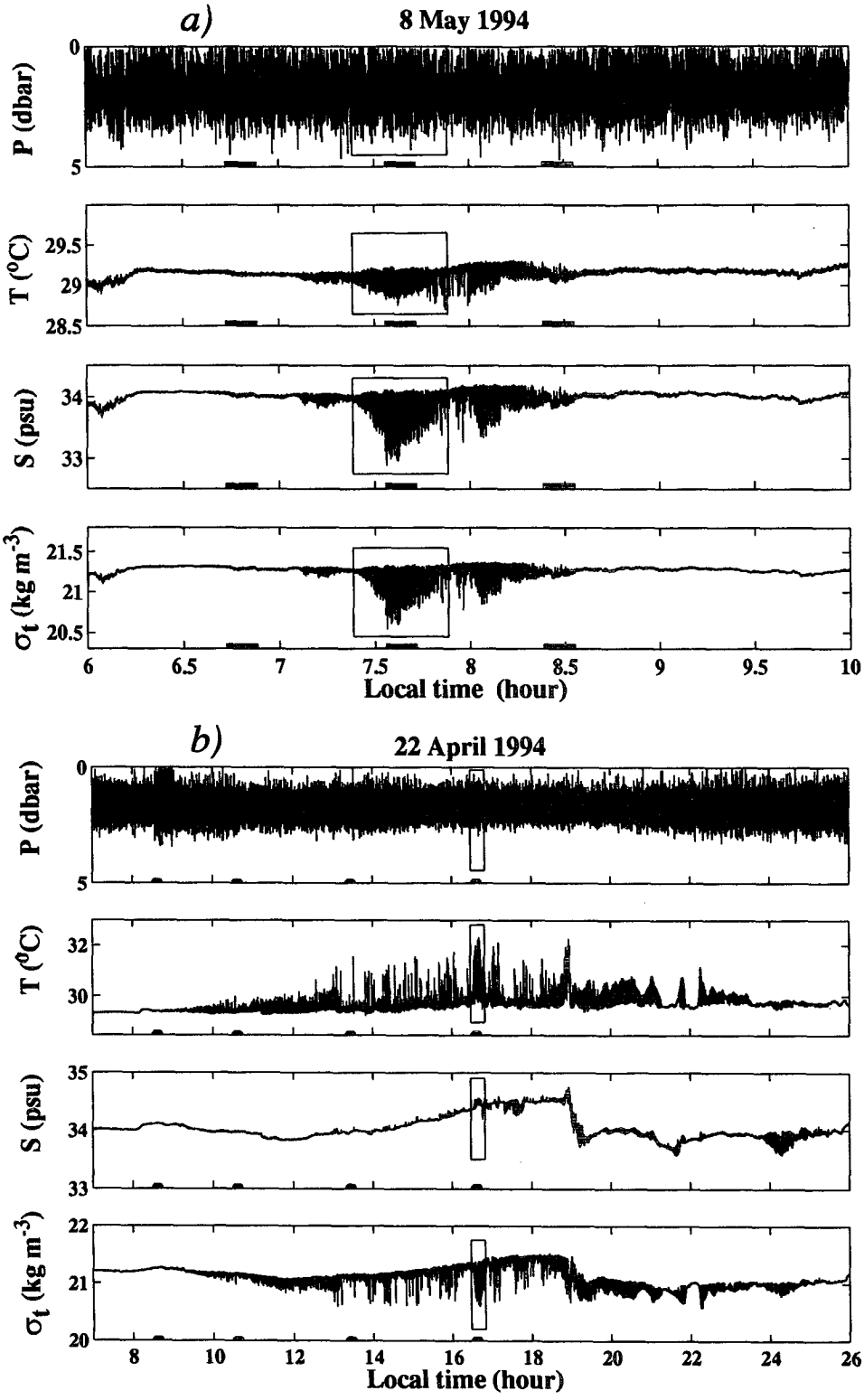

FIG. 1. Examples of records made by bow sensors in the western Pacific warm pool during a strong rain event (a) and during a strong diurnal warming event (b). Segments marked by rectangles are shown in more detail in Figs. 3 and 4. Solid segments on the time axis correspond to 10-min averaging intervals for calculation of vertical profiles of T, S, and σ_t shown in Fig. 2.

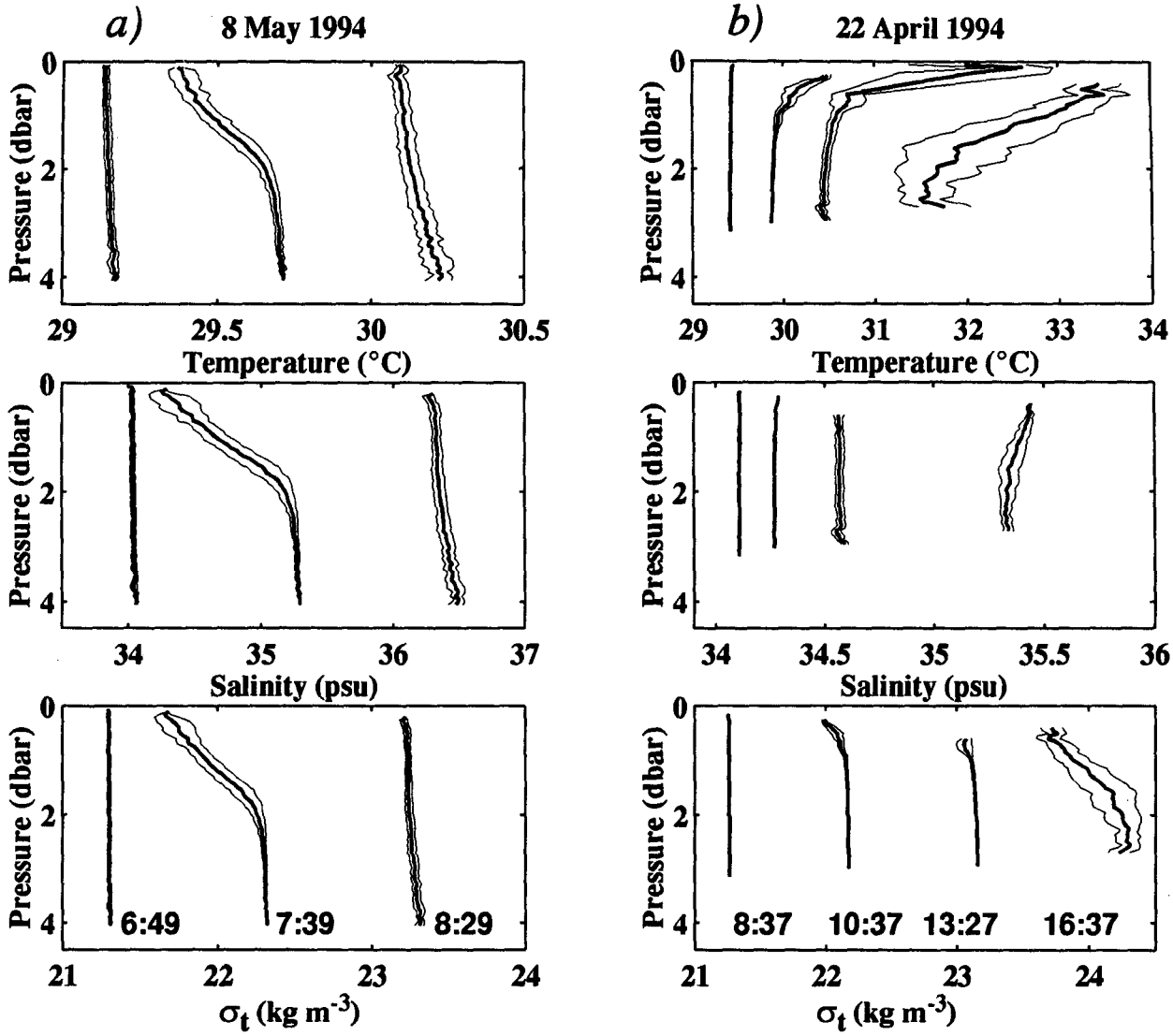

FIG. 2. Vertical profiles of temperature, salinity, and density obtained by averaging 10-min intervals of the bow sensor data within 0.1-dbar pressure ranges. Each successive profile is shifted by 0.5°C in temperature, by 1.2 psu (in subplot a) and 0.3 psu (in subplot b) in salinity, and by 1.0 in σ_t. The local time below each profile corresponds to the middle of the 10-min segment. Thin lines represent ± one standard deviation.

Averaged vertical profiles of T, S, and σ_t at 0649 (all times are LST) (Fig. 2a), measured just before entering the rain zone showed the well-mixed layer within the depth range of the bow probes. The wind speed was 7.8 m s^{-1} from 210°–240°, and there were no signatures of diurnal heating or previous rain events in the upper 4 m of the ocean. The vertical profiles at 0739 (Fig. 2a) corresponding to the core of the freshwater patch showed the strong salinity depression, $\Delta S \sim 1$ psu, localized in the upper ~2 m and accompanied by a temperature inversion of $\Delta T \sim 0.3$°C. The wind speed fluctuated strongly both in magnitude (3.2 m s^{-1}–6.9 m s^{-1}) and in direction (230°–360°) because of squalls accompanying the rain event. The σ_t vertical profile at 0739 revealed a stably stratified layer of ~2 m depth; the turbulent mixing in the near-surface layer of the ocean did not mix this strongly stratified layer. The vertical profiles at 0829 (Fig. 2a) correspond to the end of the rain zone (Fig. 1a). Stratification in the upper 4 m of the ocean is much reduced in comparison with the core of the patch. Wind speed increased up to 10–12 m s^{-1} and its direction became more stable (250°–280°).

Figure 3 gives a more detailed picture of the core of the rain patch (the T, S, and σ_t records for the corresponding segment in Fig. 1a are marked by rectangles).

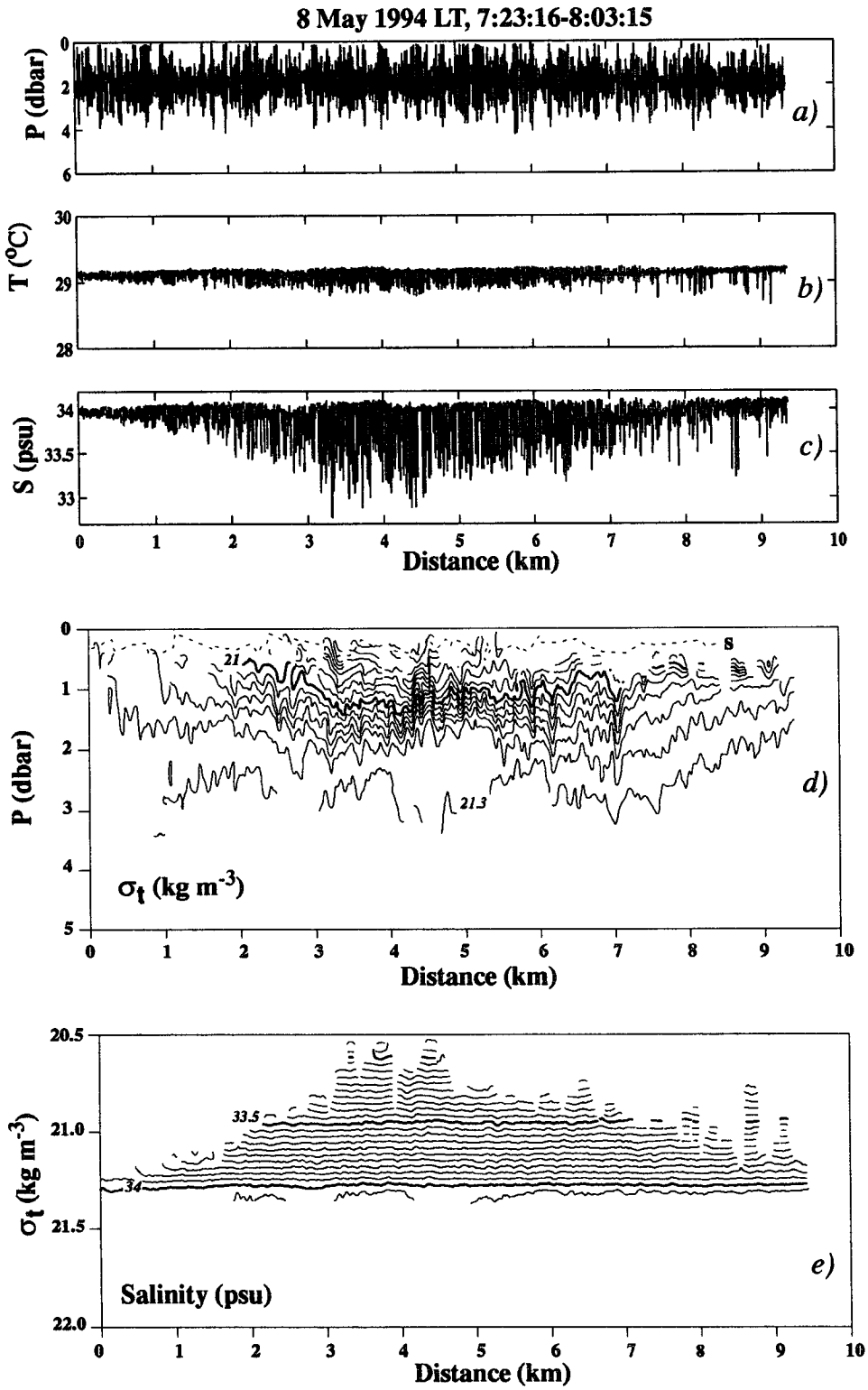

FIG. 3. Intersection of shallow freshwater patch (COARE EQ-3 leg, 4.43°N, 137.01°E). The upper part of the figure demonstrates records of (a) pressure, (b) temperature, and (c) salinity. The lower part shows (d) the corresponding contour plots of σ_t versus P and (e) S versus σ_t. The dashed line (S) in the contour plot σ_t–T corresponds to the air–sea interface as indicated by the conductivity sensor using criteria C = 4.6 S m^{-1}, where C is the conductivity. Wind speed is 3.3–6.9 m s^{-1} (rain squalls), direction 338°–353°; ship speed is 5.2 m s^{-1}, direction 1°; height of swell waves observed from the bridge ~2.5 m, direction ~030°.

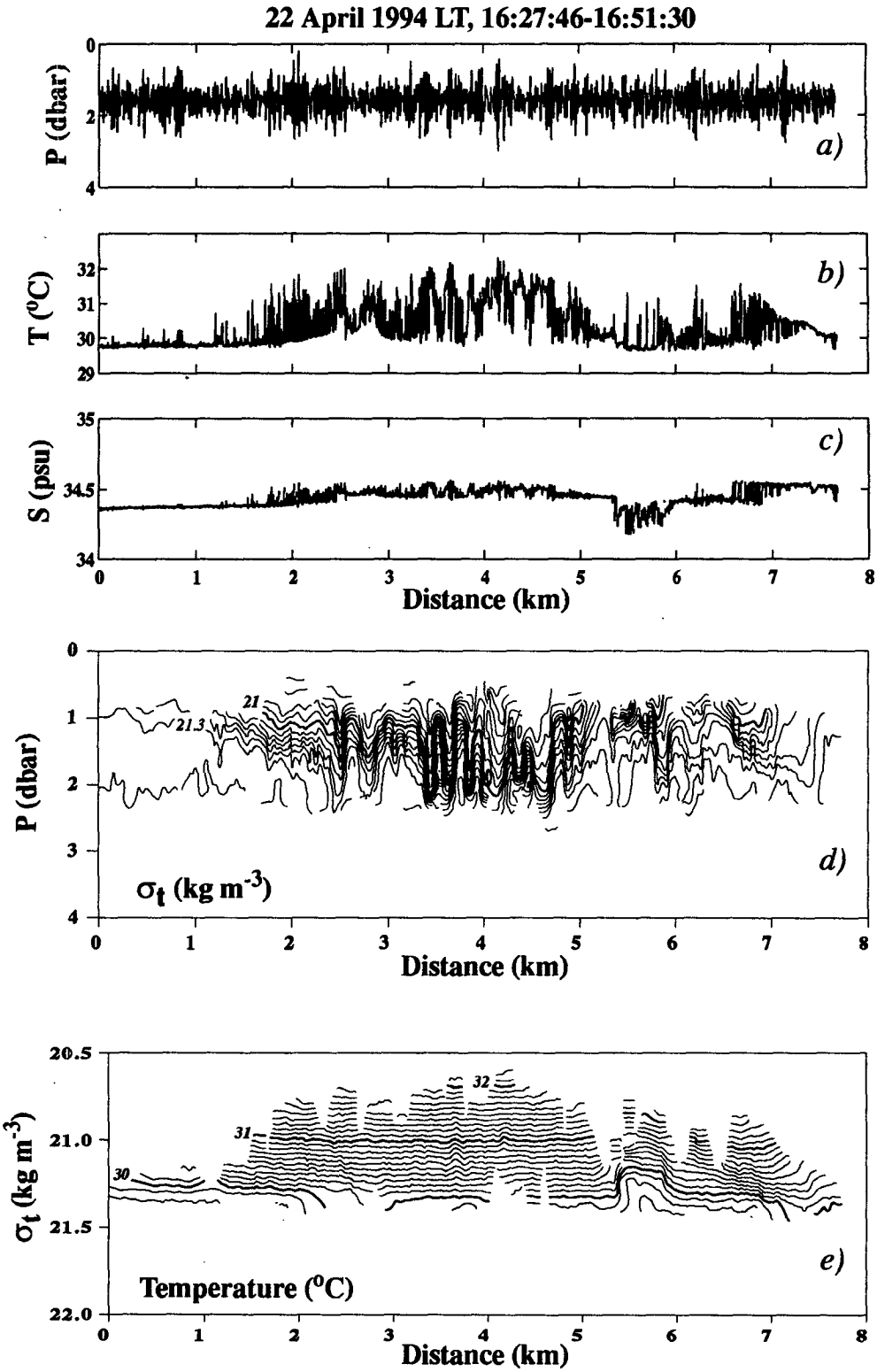

FIG. 4. Observations during strong diurnal warming (COARE EQ-3 leg, 2.2°S, 161.7°E). The upper part of the figure demonstrates records of (a) pressure, (b) temperature, and (c) salinity. The lower part shows corresponding contour plots (d) of σ_t versus P and (e) of T versus σ_t. Wind speed is 0.5–1.0 m s^{-1}, direction 297°–339°; ship speed is 5.5 m s^{-1}, direction 338°; height of swell waves observed from the bridge is ~1 m, direction ~50°.

The contour plot of σ_t versus P (Fig. 3d) reveals disturbances that look like internal waves with apparent wavelengths of ~200 m or more. The true wavelengths cannot be estimated from these measurements because the relative internal wave direction and propagation speed of the wave are unknown.

The dashed line S on contour plot $\sigma_t - P$ (Fig. 3d) corresponds to the pressure readings (the hydrostatic pressure bias has already been removed) at occasional intersections of the water–air interface as detected by the conductivity cell (see appendix). It illustrates the uncertainty of pressure to depth conversion due to the dynamical pressure component and the ~0.6 m horizontal spacing between the C, T, and P sensors. The rms uncertainty in the pressure to depth conversion is estimated as being between 0.02 and 0.1 dbar (see appendix).

The contour plot of salinity in density coordinate (Fig. 3e) shows practically no anomalies. This supports the wavelike nature of the disturbances observed on the $\sigma_t - P$ contour plot.

b. *Diurnal thermocline*

Figure 1b shows a strong diurnal warming event in the near-surface layer of the ocean. CTD profiles made before and after this section revealed the barrier layer above the thermocline with salinity difference of ~0.6 to ~1.0 psu from the top of thermocline to the base of the mixed layer. The depth of the upper quasi-homogeneous layer depth identified on the CTD temperature profiles was 40 m before and 80 m after the section. Horizontal variability of the salinity in Fig. 1b was presumably because of the previous surface forcing or the spatial variability of the underlying barrier layer. High-frequency fluctuations in T, S, and σ_t were primarily because of the depth variation of the probes.

Figure 2b demonstrates the evolution of the averaged vertical profiles of T, S, and σ_t on 22 April 1994 from early morning until late afternoon (0837, 1037, 1327, and 1637). At 0837, the profiles of T, S, and σ_t showed a well-mixed upper layer (within 3-m depth variation range of the bow sensors). Wind speed was 2.2 m s^{-1}. The temperature profile at 1037 indicated that the diurnal warming of the upper ocean layer had started. Because of low wind speed conditions (1.5 m s^{-1}), the diurnal thermocline was within the upper 1 m of the ocean. At 1327, the diurnal thermocline was still in the upper 1 m because of calm conditions (0.9 m s^{-1}). The temperature difference across it achieved ~2°C. There was also ~0.1 psu salinity difference across the diurnal thermocline as a result of evaporation from the ocean surface and accumulation of the excess salinity within the diurnal mixed layer.

Averaged vertical profiles of T, S, and σ_t at 1637 (Fig. 2b), the beginning of the evening deepening of the diurnal thermocline, reveal increased horizontal variability. This time interval is analyzed further in Fig. 4. The corresponding section of the records is denoted in Fig. 1b by a rectangle. There are high-frequency oscillations of T and S in this record (Figs. 4b and 4c) because of the depth variation of the probes. There are also variations in temperature of about 2°C in Fig. 4b, which are visible over several kilometers. The $\sigma_t - P$ contour plot (Fig. 4d) reveals wavelike disturbances of the diurnal thermocline with a typical scale beginning from ~200 m. Because the probes did not surface from 1627:46 to 1551:30, there was no opportunity to estimate uncertainty in pressure to depth conversion in the same way as we did this for the case shown in Fig. 3. Because of smaller amplitude of pitching in comparison with the case shown in Fig. 3, uncertainty in pressure to depth conversion is estimated as being <0.1 dbar.

In Fig. 4d, the amplitude of the internal disturbances is much larger than in Fig. 3d. The $T - \sigma_t$ contour plot in Fig. 4e reveals an asymmetrical anomaly between 5300 and 6000 m associated with a salinity feature (Fig. 4c). It is not clear, however, whether it is any connection between the large-amplitude short-wave train observed in the $\sigma_t - P$ contour plot (Fig. 4d) and this salinity feature.

4. Discussion

Our observations in the western Pacific warm pool reveal near-surface spatial structures that look like internal waves (Figs. 3d and 4d). For the data shown in Fig. 4d, the amplitude of the wavelike perturbations is much larger than the uncertainty of the pressure to depth conversion. Our 30-day dataset contains several cases of large amplitude internal waves within the diurnal thermocline with the amplitude comparable with the depth of the thermocline.

The $\sigma_t - P$ contour plot in Fig. 4d shows an intermittent wavelike pattern. The intermittence in space and time with energy predominantly in the first mode is a typical feature of a short-period internal wave trapped in a thermocline that is close to the surface (Brekhovskikh et al. 1975). There is also an asymmetry of the perturbations in Fig. 4d. It is typical when a thermocline is close to the surface the wave crests are flattened and the troughs become sharper (Thorpe 1968).

Voropaev et al. (1981) observed an internal wave of length ~200 m and height ~1 m in the diurnal thermocline at 5 m s^{-1} wind speed. Imberger (1985) presented detailed near-surface measurements from a freshwater lake during 21.5 hours, including observation of internal waves of amplitude ~1 m and billows associated with the diurnal thermocline. Any difference between the diurnal thermocline in the ocean and that in the lake may be because of salinity effects and different shape of the surface wave spectrum. The surface wave field is a possible source for generation of the internal mode in the diurnal thermocline by means of

the Phillips (1966) resonant mechanism. Seiching also influences the diurnal thermocline in a lake but is not typical for the open ocean.

a. *Surface waves*

Nonlinear interaction of surface gravity waves can cause the excitation of internal waves in the near-surface stratified layers. Observations of Apel et al. (1975), Briscoe (1983), and others suggest that a strong ocean swell can generate internal waves. Conditions of the resonant triad may be satisfied by a pair of surface waves with almost equal frequency and direction. The surface waves involved in the generation of the internal mode may travel from very remote regions of the ocean.

Brekhovskikh et al. (1972) and Watson et al. (1976) used a "locked phase" approximation to theoretically describe two surface waves interacting with an internal wave. This mechanism is relatively strong, predicting the internal-wave growth time of the order of a few hours. It requires, however, a rather extreme situation. Each of the two surface waves must have a deterministic phase relationship for as long as it takes to generate the internal wave. Models of "spontaneous creation mechanism" (Olbers and Herterich 1979) and "modulation mechanism" (Dysthe and Das 1981) are based on incoherent or statistical three wave interactions. According to Olbers and Herterich (1979), the spontaneous creation mechanism may play an important role if there is strong stratification. Watson (1990) concluded that, except at winds > 20 m s^{-1}, only the modulation mechanism is of practical significance (but with energy flow from the internal to surface waves). In contrast to this result for the wind waves, Watson (1990) also found that a strong, narrowband ocean swell can lead to rapid growth of high-frequency internal waves. The application of the theoretical models cited above, however, demand an advanced measurement of surface waves parameters, which is difficult to do from the ship.

b. *Diurnal jet*

The kinetic energy accumulated by the diurnal jet during a period of intensive warming is a possible source of mechanical energy for the generation of internal waves and billows in the diurnal thermocline. During a period of intensive solar heating the turbulent friction in the diurnal thermocline being controlled by the buoyancy flux at the ocean–air interface is substantially reduced (Kudryavtsev and Soloviev 1990). The diurnal jet accumulates the momentum transferred from the wind (Price et al. 1986). In the evening the net surface buoyancy flux at the ocean–air interface decreases and then becomes negative; the slippery conditions within the diurnal thermocline disappear and the momentum flux at the lower boundary of the diurnal jet increases. An increasing shear provides favorable conditions for the Kelvin–Helmholz instability that leads to breaking internal waves (Turner 1973).

The internal waves in the diurnal thermocline may result in the modulation of SST. There were observations of strong diurnal warming events near the California coast from satellite images (Flament et al. 1994). They indicated the formation of coherent streaks, associated with the erosion and decay of the warming layers, during the night following a strong diurnal warming. The horizontal spacing of the streaks observed at 1-km resolution was 4–8 km. This is consistent with Fig. 4 on which it is possible to trace a several kilometer scale variation of the near-surface temperature of ~2°C amplitude. Internal waves of wavelength ~200 m cannot be resolved on the satellite images available. The patterns between the two successive images in 5 h 26 min (Flament et al. 1994, Figs. 12b and 12c) look stationary but appear consistent with internal waves propagating at ~0.1 m s^{-1} speed in the diurnal thermocline. The corresponding ~2 km spatial deformation of the pattern cannot be clearly seen on the satellite images with 1-km space resolution.

5. Conclusions

Our observations by the bow sensors in the western Pacific warm pool indicate the presence of 0.2–6 km perturbations of the diurnal thermocline and rain-formed halocline. They are presumably related to the development of internal waves on the near-surface pycnocline. Maximum amplitude of the internal perturbations was observed during the evening deepening of the diurnal thermocline. We assume that the two mechanisms most important for the generation of the internal waves on the near-surface pycnocline are the resonant interaction between the internal mode and a pair of surface waves with almost equal frequency and direction and the shear instability produced by the diurnal jet at the evening deepening.

It is obvious that future studies should include both field and remote sensing high-resolution measurements. The internal waves in the near-surface stably stratified layers could modulate the "roughness" of the ocean surface in the same way as the internal waves in the main thermocline, making them "visible" in the SAR images and scatterometer measurements. Nonlinear internal waves and billows in the near-surface layer of the ocean associated with diurnal thermocline or rain-formed halocline may modulate SST producing specific spatial patterns seen in the thermal infrared images.

Acknowledgments. Michael Gregg suggested the inclusion of measurements in near-surface layer of the ocean to the TOGA COARE planners. Bob Weisberg, Rick Cole, and Linda Mangum kindly included the measurements in the program of MW9410 and

MW9411 COARE cruises of the R/V *Moana Wave*. Mark Baker provided testing and post-calibration of the bow probes. Anatoli Arjannikov and Jefrey Snyder provided technical support for the measurements and pre-cruise calibration of the instrumentation. Sharon DeCarlo and Dmitry Khlebnikov wrote the software for recording and preliminary processing of the data. The assistance of the crew of the R/V *Moana Wave* was crucial for success of the program. We thank Lou Goodman for the useful discussion of the results. The study was supported by the U.S. National Science Foundation (Grants OCE-9216891 and OCE-9113948), the Office of Naval Research, and by the Russian Academy of Sciences.

APPENDIX

Estimation of Pressure to Depth Conversion Uncertainty

a. Estimate of the dynamical pressure influence

The pressure signal is equal to

$$P = P_d + P_h. \tag{A1}$$

The hydrostatic component P_h is used to calculate the depth of the probe. The dynamical component P_d depends on the relative flow. The orbital velocities of the surface waves and the ship's pitching produce fluctuations of the relative flow that affect the dynamical pressure. To reduce the influence of the dynamical component, the pressure sensor is installed in the tail section of the ECTP probe.

The dynamical component is assumed to be governed by

$$P_d = C_d \rho U^2/2, \tag{A2}$$

where C_d is the nondimensional proportionality coefficient, U is the magnitude of the relative flow velocity, and ρ is the density of the medium. The value of C_d depends on the hydrodynamic form of the bow sensor and on the relative flow direction. In the air, the dynamical component vanishes because density ρ drops from $\sim$1024 kg m^{-3} (water density) to $\sim$1.2 kg m^{-3} (air density).

The sudden conductivity signal change at the ocean–air interface is an indication of the conductivity cell surfacing. The conductivity cell is installed in the front section of the ECTP, along its axis line. The pressure sensor is installed in the tail part of the ECTP at a distance of L_a = 0.06 m below the axis line. The conductivity sensor actually indicates the air–sea interface when the distance to the surface is equal to the spatial resolution of the conductivity cell ($L_s \sim 0.1$ m). An empirical criteria,

$$C = C_s \tag{A3}$$

was used as an indicator of the surfacing. The conductivity signal is C, and C_s = 4.6 S m^{-1}. The pressure readings at the occasional intersections of the water–air interface as detected by the conductivity signal using the above criteria are interpolated on contour plot $\sigma_t - P$ in Fig. 3d by dashed line S.

The dynamical component can be estimated from (A1):

$$P_d = P|_{C=C_s} - P_h|_{C=C_s}, \tag{A4}$$

where $P|_{C=C_s}$ is the pressure signal at the surfacing. The hydrostatic pressure at the surfacing is equal to $P_h|_{C=C_s} = \rho g L_a + \rho g L_s$. For the observations shown in Fig. 3, the mean value of the dynamical pressure estimated from (A4) is equal to 0.14 dbar.

The most complicated factor of the pressure to depth conversion is the variation of the dynamical pressure rather than its mean value. Assuming constant values of C_d and ρ in (A2), the variation of the dynamical pressure ΔP_d can be estimated in the following way:

$$\frac{\Delta P_d}{P_d} = \frac{2\Delta U}{U}, \tag{A5}$$

where ΔU is the variation of relative flow speed U. For the case shown in Fig. 3, the relative-flow rms speed variation measured by the longitudinal V_x velocity sensor (EMVA probe) is equal to $\Delta U/U_0 = 0.08$. An rms estimation of the dynamical pressure fluctuation from (A5) is then equal to $\sim$0.02 dbar. The dynamical pressure fluctuations in the tail segment of the ECTP probe may be stronger than calculated from (A5) because C_d depends on the relative flow angle. The relative flow angle varies because of the orbital velocities of the surface waves and the ship's pitching. The 0.6-m horizontal separation between the conductivity cell and the pressure sensor also results in some uncertainty in relative positions of the sensors with respect to the air–sea interface at the probes' surfacing. This method therefore underestimates the uncertainty in the pressure to depth conversion.

Another estimate can be obtained by calculating the rms pressure variation at the surfacing, using the dynamical pressure determined by (A4). For the observations shown in Fig. 3, it is equal to 0.096 dbar. Such a method, however, overestimates the uncertainty in the pressure-to-depth conversion. When the conductivity sensor indicates the sea surface, the pressure sensor is normally in the water. The instances when the pressure sensor was in the air when the conductivity sensor indicated the interface, however, are not excluded because of the random slope of the sea surface with respect to the ECTP axis line. When this occurs, the dynamical pressure jumps practically to zero, producing additional fluctuations of the pressure signal.

For the case shown in Fig. 3, pitching was one of the most severe in the EQ-3 cruise. Its range in the area of the bow sensors was $\sim$4 m. For other measurements in EQ-3 (including the example shown in Fig. 4), the uncertainty in the pressure to depth conversion should

be lower because of the smaller relative flow speed variation.

b. *Correlation estimate*

Because of the dynamical pressure component, the amplitude alteration of the ship's pitching might result in an "artificial" wavelike pattern on the contour plots. However, any statistically significant correlation between the envelope of the P oscillation (because of the ship's pitching and the surface waves) and the σ_t values within 0.1-dbar pressure ranges was not found. The corresponding correlation coefficient averaged over all depth ranges was equal to -0.01 for the data shown in Fig. 3d and -0.05 for the data shown in Fig. 4d.

REFERENCES

Anderson, S. P., R. A. Weller, and R. Lukas, 1996: Surface buoyancy forcing and the mixed layer of the western Pacific warm pool: O1D model results. *J. Climate,* in press.

Apel, J. K., H. M. Byrne, J. R. Proni, and R. L. Charnell, 1975: Observations of oceanic internal and surface waves from the Earth Resources Technology Satellite. *J. Geophys. Res.,* **80,** 865–881.

Brainerd, K. E., and M. C. Gregg, 1993: A comparison of length scale and decay times of turbulence in the ocean surface mixed layer. 2. Modeling. *J. Geophys. Res.,* **98,** 22 657–22 664.

Brekhovskikh, L. M., V. V. Goncharov, V. M. Kurtepov, and K. A. Naugol'nykh, 1972: Resonant excitation of internal waves by nonlinear interaction of surface waves. *Izv. Atmos. Ocean. Phys.,* **8,** 192–203.

——, K. V. Konjaev, K. D. Sabinin, and A. N. Serikov, 1975: Short-period internal waves in the sea. *J. Geophys. Res.,* **80,** 856–864.

Briscoe, M. G., 1983: Observations on the energy balance of internal waves during Jasin. *Philos. Trans. Roy. Soc. London,* **A308,** 427–444.

Bruce, J. G., and E. Firing, 1974: Temperature measurements in the upper 10 m with modified expendable bathythermograph probes. *J. Geophys. Res.,* **79,** 4110–4111.

Dysthe, T. H., and K. P. Das, 1981: Coupling between a surface wave spectrum and an internal wave: Modulation interaction. *J. Fluid Mech.,* **104,** 483–503.

Farmer, D. M., and J. R. Gemmrich, 1996: Measurements of temperature fluctuations in breaking surface waves. *J. Phys. Oceanogr.,* **26,** 816–825.

Flament, P., J. Firing, M. Sawyer, and C. Trefois, 1994: Amplitude and horizontal structure of a large diurnal sea surface warming event during the coastal ocean dynamics experiment. *J. Phys. Oceanogr.,* **24,** 124–139.

Fozdar, F. M., G. J. Parker, and J. Imberger, 1985: Matching temperature and conductivity sensor response characteristics. *J. Phys. Oceanogr.,* **15,** 1557–1569.

Imberger, J., 1985: The diurnal mixed layer. *Limnol. Oceanogr.,* **30,** 737–770.

Kudryavtsev, V. N., and A. V. Soloviev, 1990: Slippery near-surface layer of the ocean arising due to daytime solar heating. *J. Phys. Oceanogr.,* **20,** 617–628.

Lukas, R., and E. Lindstrom, 1991: The mixed layer of the western equatorial Pacific Ocean. *J. Geophys. Res.,* **96**(Suppl.), 3343–3358.

Olbers, D. J., and K. Herterich, 1979: The spectral energy transfer from surface waves to internal waves. *J. Fluid Mech.,* **92,** 349–380.

Phillips, O. M., 1966: *The Dynamics of the Upper Ocean.* Cambridge University Press, 261 pp.

Price, J., R. Weller, and R. Pinkel, 1986: Diurnal cycling: Observations and models of the upper ocean response to diurnal heating, cooling and wind mixing. *J. Geophys. Res.,* **91**(C7), 8411–8427.

Shinoda, T., S. DeCarlo, S. Kennan, R. Lukas, F. Santiago-Mandujano, and J. Snyder, 1995: Shipboard measurements during COARE Enhanced Monitoring Cruises. SOEST Tech. Rep. 95-07, School of Ocean and Earth Science and Technology, University of Hawaii, Honolulu, HI, 205 pp.

Smyth, W. D., P. O. Zavialov, and J. N. Moum, 1995: Decay of turbulence in the upper ocean following sudden isolation from surface forcing. *J. Phys. Oceanogr.,* in press.

Soloviev, A. V., and N. V. Vershinsky, 1982: The vertical structure of the thin surface layer of the ocean under conditions of low wind speed. *Deep-Sea Res.,* **29,** 1437–1449.

——, R. Lukas, S. DeCarlo, J. Snyder, A. Arjannikov, M. Baker, and D. Khlebnikov, 1995: Small-scale measurements near the ocean–air interface during TOGA COARE. Data Rep. SOEST 95-05, University of Hawaii, Honolulu, HI, 257 pp.

Thorpe, S. A., 1968: On the shape of progressive internal waves. *Philos. Trans. Roy. Soc. London,* **A263,** 563–614.

——, 1995: Dynamical processes at the sea surface. *Progress in Oceanography,* Vol. 35, Pergamon, 315–352.

Turner, J. S., 1973: *Buoyancy Effects in Fluids.* Cambridge University Press, 367 pp.

Voropaev, S. I., B. L. Gavrilin, and A. G. Zatsepin, 1981: On the structure of the surface layer of the ocean. *Izv. Akad. Nauk SSSR, Atmos. Oceanic Phys.,* **17,** 378–382.

Watson, K. M., 1990: The coupling of surface and internal gravity waves: Revisited. *J. Phys. Oceanogr.,* **20,** 1233–1248.

——, B. J. West, and B. I. Cohen, 1976: Coupling of surface and internal gravity waves: A mode coupling model. *J. Fluid Mech.,* **77,** 185–208.

Webster, P. J., and R. Lukas, 1992: TOGA COARE: The Coupled Ocean–Atmosphere Response Experiment. *Bull. Amer. Meteor. Soc.,* **73,** 1377–1416.